



Fe-MOF derivative photocatalyst with advanced oxygen reduction capacity for indoor pollutants removal

Junxian Qin^a, Yun Pei^a, Yue Zheng^a, Daiqi Ye^{a,b,c}, Yun Hu^{a,b,c,*}

^a School of Environment and Energy, South China University of Technology, Guangzhou 510006, PR China

^b Guangdong Provincial Key Laboratory of Atmospheric Environment and Pollution Control, Guangzhou 510006, PR China

^c The Key Lab of Pollution Control and Ecosystem Restoration in Industry Clusters, Ministry of Education, Guangzhou 510006, PR China

ARTICLE INFO

Keywords:

Metal organic framework derivative
Photocatalysis
Volatile organic compounds
Bacteriostat
Oxygen reduction

ABSTRACT

Fe-MOF derivative (M-300) is successfully prepared by thermal treatment using MIL-100(Fe) as a precursor. The resulting M-300 catalyst displays excellent performance in the degradation of volatile organic compounds (VOCs) and the bacteriostasis to *Escherichia coli* under the visible light. In addition, the catalyst also exhibits the capacity of acetaldehyde degradation under actual sunlight. The high activity is attributed to the abundant exposure of the unsaturated Fe²⁺ active site, which can significantly promote the transfer of photogenerated electron and the oxygen reduction process, thus improving the efficiency of the entire photocatalytic oxidation reaction. This work shows the application prospect of MOFs derivatives in the field of indoor photocatalytic purification, and also provides a new insight into the study of catalyst modification in photocatalytic degradation of pollutants.

1. Introduction

People spend most of their time indoors, so indoor environmental quality has a huge impact on human health. The main indoor pollutants include volatile organic compounds (VOCs) and pathogens. At present, the main ways to remove the indoor pollutants is adsorption. However, the adsorption performance is easily affected by temperature [1,2]. Photocatalysis is considered as an ideal indoor air purification technology due to its non-toxic, economy and fewer restrictions [3–5]. But the traditional photocatalyst TiO₂ is suffers from its narrow photo-activity range in ultraviolet light and the recombination of photogenerated electrons and holes, which are seriously hindering the application of photocatalysis. Therefore, it is necessary to develop an efficient photocatalyst suitable for indoor air purification.

As a new type of porous materials, metal-organic frameworks (MOFs) are widely used in adsorption, separation and catalysis due to their uniform distribution of active sites and high porosity [6–8]. MOFs are not only great materials enriched with a large specific surface area, but also ideal semiconductors for photocatalysis. Highly dispersed and controllable metal sites on MOFs can be used as photocatalytic active sites to achieve the enrichment and removal of the pollutants. However, the structure of MOFs is vulnerable for its poor chemical stability during

the photocatalysis, which makes it difficult to be applied into actual photocatalytic degradation of pollutants [9,10].

In order to solve this defect, MOFs derivatives have attracted increasing attention in recent years, and have been applied in the field of environmental catalysis because of their stable structure and uniform activity sites inheriting from their MOFs precursor [8,11–14]. For example, Chen et al. obtained photocatalyst with more Ti³⁺ and oxygen vacancies by calcination of Ti-MOF to degrade the tetracycline in actual water [15]; Zhang et al. calcined ZIF-L to obtain N-ZnO derivatives with more oxygen vacancies to improve the degradation efficiency of lenofloxacin [16]. In the above photocatalytic reactions, the catalysts are excited by irradiation to generate the electrons and holes. The photogenerated holes oxidize the pollutants or produce the reactive oxygen species (ROS), and the photogenerated electrons reduce the electron acceptors. However, most of the researches in the field of photocatalytic oxidation are focused on the mechanism of oxidation half-reaction, and there is a lack of in-depth research on the reduction process. That leads to the incomplete researches on the photocatalytic mechanism [17]. In most photocatalytic degradations, O₂ is the only electron acceptor. In our previous research, TiO₂ modified with a MOF (ZIF-8) derivative GC-N could promote the transfer of photogenerated electrons to O₂, thus greatly improved the photocatalytic oxidation activity for toluene [14].

* Corresponding author at: School of Environment and Energy, South China University of Technology, Guangzhou 510006, PR China.

E-mail address: huyun@scut.edu.cn (Y. Hu).

<https://doi.org/10.1016/j.apcatb.2022.122346>

Received 31 October 2022; Received in revised form 26 December 2022; Accepted 29 December 2022

Available online 31 December 2022

0926-3373/© 2023 Elsevier B.V. All rights reserved.

This indicated that improving the reduction efficiency of O_2 is also one of the effective strategies to promote the removal of pollutants.

Fe-based MOFs are one of the most attractive materials due to the abundance and the chemical activity of Fe element [18,19]. MIL-100 (Fe) is one of the representatives of Fe-MOF which is combined with ferric oxygen clusters and carboxylate. However, during the synthesis, the electrons at the Fe sites are easily coordinated with H_2O or anions (OH^- , F^-), which limits the activity of MIL-100(Fe) [20]. To enhance the catalytic activity of MIL-100(Fe), we propose a thermal treatment strategy to remove the pre-coordinated impurities and obtain the MIL-100(Fe) containing unsaturated Fe sites [21]. These unsaturated sites greatly promote the interaction between MOFs and reactants, leading to higher adsorption and catalytic performance [22]. As a consequence, MIL-100(Fe) derivative is an attractive candidate for oxygen-reduced half-reaction in photocatalysis of pollutant removal.

In this study, drawing on our previous reports on MOFs derivatives [14,21], MIL-100 (Fe), a Fe-MOFs with abundant Fe sites, was selected as the precursor. Fe-MOF derivatives with higher surface area, hierarchical pore structure and structural stability were obtained by thermal treatment in N_2 atmosphere. Acetaldehyde and *Escherichia coli* (*E. coli*) were chosen as typical indoor model pollutants for photocatalytic oxidation activity test. In addition, the photocatalytic performance under actual sunlight was investigated. By controlling the heating temperature, the unsaturated Fe^{2+} sites could be regulated to increase transfer rate of photogenerated electrons to O_2 , thus greatly promoting the removal performance of pollutants. In addition, the photocatalytic mechanism was revealed at molecular level by probe experiment, poisoning experiment, and in-situ ORR characterization.

2. Experimental method

2.1. Materials

Reduced iron powder, 1,3,5-benzenetricarboxylates (H_3BTC), hydrofluoric acid (HF) and nitric acid (HNO_3) were purchased from Aladdin Reagent Co., Ltd. Acetone were supplied by Sinopharm Chemical Reagent Co., Ltd, China. Fe_2O_3 was bought from Shanghai Macklin Biochemical Co., Ltd. Plate count agar and LB broth were obtained from Guangdong Huankai Microbial Sci. & Tech. Co., Ltd. All chemicals and reagents were analytical grade and used without further purification.

2.2. Preparation of samples

Synthesis of MIL-100: the synthesis was based on the previous reported [21]. 0.56 g of reduced iron powder, 1.4 g of H_3BTC , 500 μL of 40 % HF and 475 μL of 65 % HNO_3 were added in 50 mL of deionized water and stirred for 1 h at room temperature. Then the mixture was transferred to a 100 mL Teflon-lined stainless steel autoclave reactor and subjected to hydrothermal treatment at 150 °C for 12 h. After cooling to room temperature, the MIL-100 was collected by centrifugation and washed by deionized water. The resultant MIL-100 was further purified in deionized water at 80 °C for 3 h and subsequently in ethanol at 60 °C for 3 h, and dried at 60 °C overnight.

Synthesis of MIL-100 derivative: MIL-100 derivative was obtained by thermal treatment MIL-100(Fe) in a N_2 atmosphere at certain temperature for 3 h with a 1 °C/min rate. The derivative labeled as M-T, where T was the temperature of thermal treatment.

2.3. Characterizations

The as-obtained catalysts were characterized by scanning electron microscope (SEM), XRD, FTIR, Raman, the element analysis of C, H, O, UV-vis, X-ray photoelectron spectrometer (XPS), photoelectrochemical measurements, temperature-programmed desorption of CO (CO-TPD), electron spin-resonance spectroscopy (ESR). A more detailed description of the different characterizations is given in the [Supporting information](#).

2.4. Evaluation of photocatalytic activity

The photocatalytic performance of VOCs degradation was conducted in a closed-circulation reactor at ambient conditions (Fig. S1a) [14]. The catalyst films were obtained by dispersing 25 mg of samples in 0.5 mL ethanol and stirring for 30 min then coating on a 2×2.5 cm aluminum foil. The prepared photocatalyst films were then dried at 100 °C overnight in air to remove the residual ethanol. The volume of the reactor was 100 mL with a quartz window having a diameter of 5 cm. A magnetic bar was placed at the bottom to mix the air in the reactor. As shown in Fig. S1b, the concentration of VOCs (acetaldehyde, acetone) was adjusted by bubbling N_2 through the liquid (acetaldehyde, acetone). The relative humidity was 60%. VOC concentration was determined with a flame ionization detector (FID) of gas chromatograph (GC-9790 II, FULI) by injecting 1 mL of gas sample. And CO_2 concentration was determined with an FID combining a methanizer of gas chromatograph (GC-6600, FANWEI) by the same way. When the concentration in the reactor was stable at the target, the inlet and outlet were closed, and then the light was turned on for experiment. A UV-cutting filter-xenon-lamp (Perfectlight, PLS-SXE300/300UV) was used as a light source. The intensity of visible light was 20 mW/cm² measured by a power meter (Cealight, CEL-NP2000).

2.5. Evaluation of antibacterial activity

E. coli (ATCC 8099) was used as the model bacterium. The bacteria grown in the LB broth at 37 °C, cultured to the log phase with shaking for 12 h. The bacteria were collected by a centrifugation at 8000 rpm min⁻¹ and washed by normal saline (0.9 %) several times and then suspended in 100 mL normal saline labeled as *E. coli* solution. Then 100 mg of MIL-100(Fe) and M-300 were dispersed in 100 mL of normal saline, respectively, and 1 mL of *E. coli* solution was added. And then the solutions were irradiated by a 300 W xenon-lamp (Perfectlight, PLS-SXE300/300UV) with a light filter of $\lambda < 420$ nm for 5 h. The intensity of light was 150 mW/cm². The group of without catalysis was labeled as blank. The bacterial concentration was measured by standard spread-plating techniques [23]. Each sample was gradiently diluted and each dilution in duplicate was plated onto the plate count agar culture medium and incubated at 37 °C for 12 h. Bacteria removal rate was calculated using the following equation:

$$\text{removal\%} = \frac{C_0 - C}{C_0} \times 100\%$$

where C is the concentration of bacteria after the irradiation and C_0 is the concentration before the irradiation of the experiments.

2.6. Evaluation of photocatalytic activity under the sunlight

The catalyst films were obtained by dispersing 100 mg of samples in 2 mL ethanol and stirring for 30 min then coating on a culture medium with 10 cm diameter. The prepared photocatalyst films were then dried at 100 °C overnight in air to remove the residual ethanol. The volume of reactor was 12 L with a steel glass window cover, sealed by vacuum silicone. A fan was placed to mix the air in the reactor (Fig. S2). A contain of acetaldehyde liquid was injected and volatilized overnight, the concentration was 60 ppm. The products were measured by gas chromatograph (GC-9790 II, FULI).

2.7. Measurement of radical species

The measurements of radical species were similar to our previous report [14].

Hydroxyl radical ($\bullet OH$) was determined by coumarin. It could react with $\bullet OH$ and generate 7-hydroxycoumarin (7-HC). 20 mg of catalyst was added to the 100 mL of solution containing the coumarin (0.3 mM)

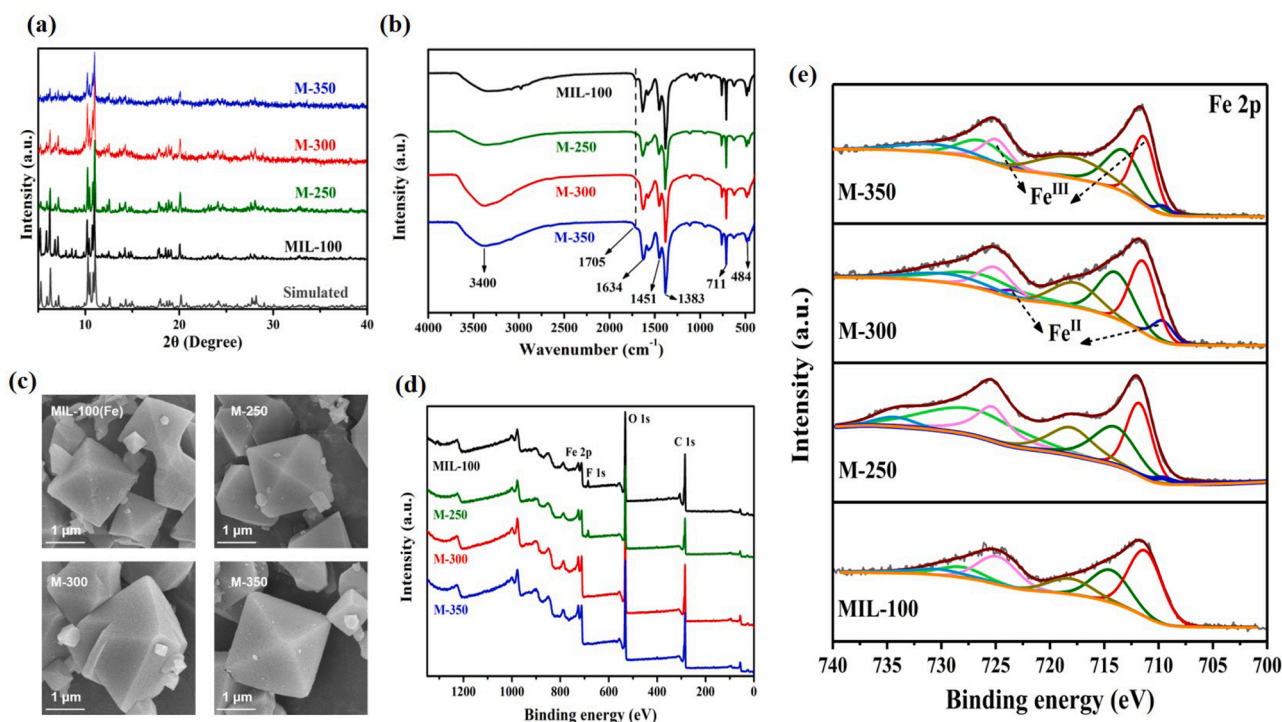


Fig. 1. (a) XRD patterns, (b) FT-TR spectra, (c) SEM images, (d) XPS spectra and Fe 2p XPS spectra of the different samples.

with ultrasonic dispersion for 5 min. The solution was then stirred for 30 min in the dark. Next, the suspension was kept stirred under ambient conditions and irradiated for 1 h. The suspensions were sampled filtered to remove the particles. The production of 7-HC was estimated by monitoring the emission intensity at 455 nm excitation at 332 nm, using a spectrofluorometer (Hitachi, F-7000).

Superoxide radical ($O_2^{\bullet-}$) was determined by nitrotetrazolium blue chloride (NBT). NBT could react with ($O_2^{\bullet-}$) and form blue particles. 20 mg of sample was added in 40 mL of NBT solution (60 μ M). The experiment process was similar to that used in the \bullet OH-measurement. The production of $O_2^{\bullet-}$ was analyzed by detecting the concentration of NBT with a Thermo Evolution 300 spectrophotometer at 259 nm.

H_2O_2 could be determined by $KMnO_4$. 20 mg of catalyst was added to 100 mL of solution containing 0.4 mM $KMnO_4$. The testing process was similar to above measurement. The concentration of MnO_4^- was determined with a Thermo Evolution 300 spectrophotometer at 525 nm.

2.8. Evaluation of poison experiment

At room temperature, CO did not have strong interaction with Fe^{3+} but easily poisoned the Fe^{2+} sites [24]. A typical poisoning process was carried out in this way: a certain of samples was mixed with 0.2 g of quartz sand and put into quartz tube. Then the sample adsorbed CO under a steam of 10 % CO at room temperature over 12 h. Then the poisoned samples were prepared as catalyst films. The photocatalytic experiment of poisoned sample was same as above experiment of photocatalytic activity.

3. Results and discussion

3.1. Structural and morphological characterizations

The crystallinity and structure of the samples were analyzed by XRD. As shown in Fig. 1a, pure MIL-100(Fe) showed high crystallinity, and the diffraction peak was consistent with the simulated pattern, indicating the successful synthesis of MIL-100(Fe). For the derivatives, the diffraction patterns of M-250, M-300 and M-350 did not change

compared with MIL-100(Fe), showing that the crystal structures of the derivatives were not changed during thermal treatment.

The FT-IR spectra showed the functional group on the surface of samples (Fig. 1b). The wide absorption band located around 3400 cm^{-1} was attributed to the O-H vibration of the adsorbed water on the surface [7]. The peaks at 1383 , 1451 , and 1634 cm^{-1} corresponded to the symmetric and asymmetric vibrations of the carboxyl linker [25,26]. The peak at 711 cm^{-1} was the C-H stretching vibration of the aromatic ring, while the peak at 484 cm^{-1} was due to the stretching vibration of Fe-O [27]. The characteristic peaks of the derivatives were similar to those of MIL-100(Fe), indicating that the functional groups of the samples were less affected by thermal treatment. In addition, the peak at 1705 cm^{-1} was attributed to the C=O vibration of the unreacted organic linker [28,29]. Compared with MIL-100(Fe), the intensity of M-250, M-300 and M-350 at 1705 cm^{-1} were significantly reduced, showing that the impurities on the catalyst surface could be further removed during the thermal treatment.

The morphology was analyzed by SEM (Fig. 1c). MIL-100(Fe) exhibited regular octahedral structure and smooth surface. For the derivatives, the octahedral shapes were well maintained, indicating that the thermal treatment did not cause obvious structural collapse. Fig. S3 showed the color change of the sample, MIL-100(Fe) was light orange, and with the increase of heating temperature, the color of the samples gradually became darker. M-250 and M-300 showed yellowish brown, while M-350 was dark brown, which may be caused by the carbonization of organic skeleton.

Raman spectrum was carried out to investigate the degree of carbonization, the intensity of the G peak at around $1580\text{--}1600\text{ cm}^{-1}$, corresponding to the graphite phase of carbon (Fig. S4). M-300 and M-350 obtained by higher temperature of thermal treatment had higher intensity of G peak, which indicated that they had higher degree of carbonization than MIL-100(Fe) and M-250. To further compare the degree of carbonization of M-300 and M-350 quantitatively, the element analysis of C, H, and O atoms was evaluated to calculate the atom ratios of H/C and O/C. As shown in van Krevelen diagram, the H/C and O/C ratios of M-350 were lower than that of M-300. It meant that M-350 had higher degree of carbonization (Fig. S5) [30].

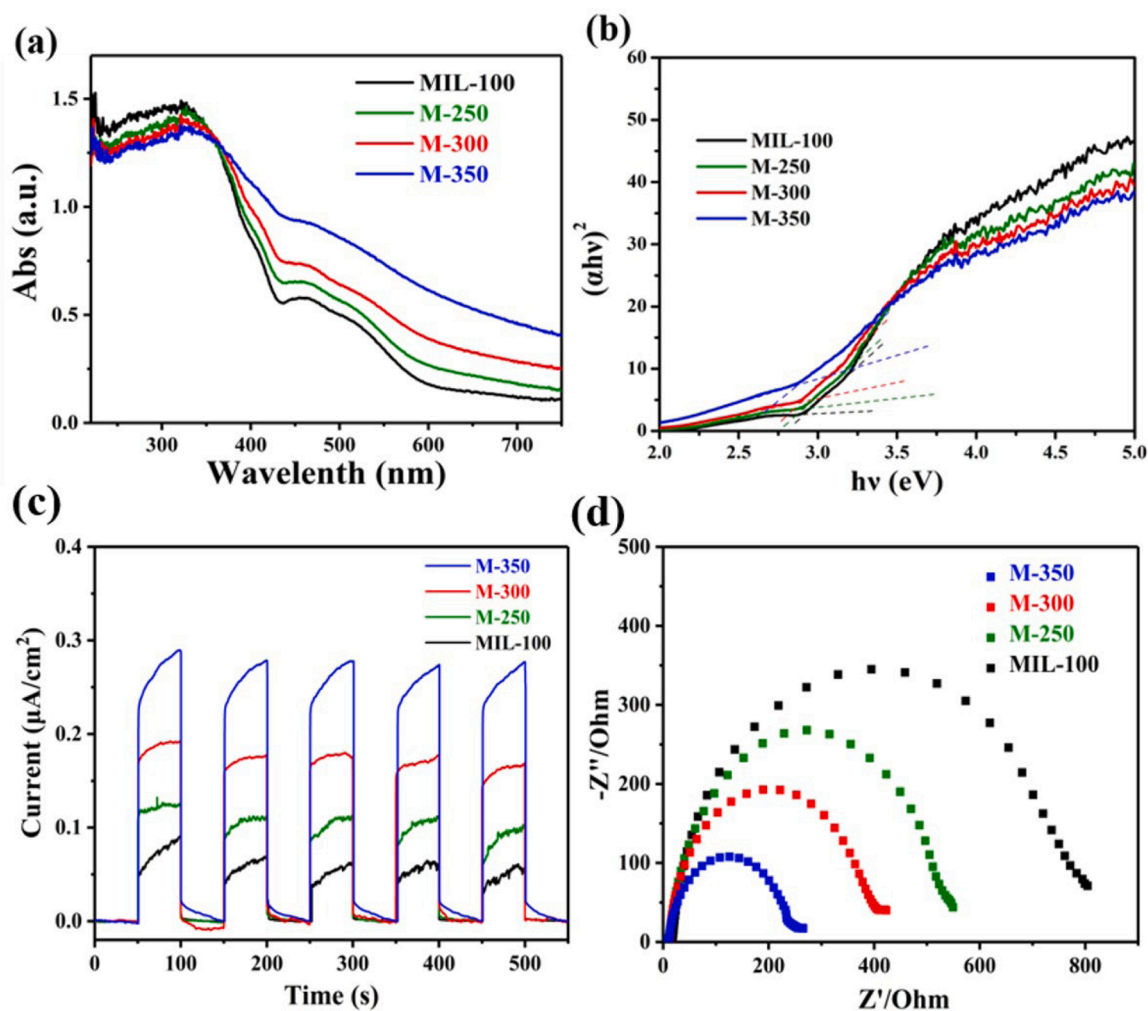


Fig. 2. (a) UV-vis spectra and (b) Tauc plots of the different samples; (c) photocurrent transient response and (d) EIS Nyquist plots of the different samples.

Fig. 1d displayed the XPS spectra of the different samples, the signals of C, O, Fe, and F could be found on the surface of samples. The F element came from the HF during the synthesis process and combined with Fe, forming the Fe-F band. After modified at high temperature, the F 1s peak gradually decreased, and the F 1s signal almost disappeared in the spectra of M-300 and M-350. This indicated that the Fe-F bond broke due to high temperature over 300 °C [31]. The result of Fe 2p spectra was ascribed to Fe 2p_{3/2} and Fe 2p_{1/2} at around 711.4 and 725.1 eV, respectively (Fig. 1e). The fitting peaks at 714.7, 718.5, 728.7 and 730.7 eV were attributed to Fe³⁺, which indicated that the Fe in MIL-100(Fe) was mainly Fe³⁺ [32,33]. Fitting peaks located at 709.6 and 723.2 eV were observed in M-250, M-300 and M-350, which corresponded to the characteristic peaks of Fe²⁺ [33,34]. Besides, the XPS peak area ratio of Fe²⁺/Fe³⁺ was used as a reference to the content ratio of Fe²⁺/Fe³⁺, as shown in Table S1, the Fe²⁺/Fe³⁺ ratio in M-250 did not increase much, which was 0.075, while M-300 had the highest Fe²⁺/Fe³⁺ ratio of 0.250. It was worth noting that the Fe²⁺/Fe³⁺ ratio of M-350 decreased with the further increased of temperature. That might be due to the excessive carbonization of organic skeleton, leading to the Fe agglomeration in Fe-O clusters [35,36]. These meant that a proper temperature was critical to the formation of abundant Fe²⁺.

MIL-100(Fe) is built up from the trimers of iron octahedra and the H₃BTC. Each Fe center is coordinated by O donor atoms from four carboxylate groups and a common vertex μ_3 -O, remaining an open metal site (Scheme S1) [37]. Therefore, MIL-100(Fe) has Fe atoms in the +2-oxidation state and has coordinatively unsaturated metal sites

theoretically [38]. But these unsaturated active sites are priorly occupied by -OH or -F during the synthesis process. Although the bonds of Fe-OH or Fe-F are hard to be broken under ambient temperature, they can be removed by thermal treatment at around 300 °C. Combined with the characterization results of F 1s spectra, the increase of unsaturated Fe²⁺ sites might result from the breaking of Fe-F bond during the thermal treatment.

3.2. Photoelectrochemical properties

The photocatalytic performance of the samples was related to their light response capacity. UV-vis spectroscopy was conducted. Fig. 2a showed the UV-vis spectra of different samples. The photo response in the ultraviolet region could be attributed to the " π - π " transition of organic ligands, while the photo response in the visible region could be related to the electron transfer from organic ligands to metal, and might also be attributed to the excitation of Fe-O clusters [39,40]. At the same time, the thermal treatment affected the absorbance. With the increased of temperature, compared with the precursor MIL-100(Fe), the ultraviolet absorbances of the derivatives gradually decreased, which were related to the increasing carbonization that impaired the " π - π " transition of the organic ligand. More importantly, the absorbance in the visible region was greatly enhanced, and the absorption edge was gradually red-shifted, which might be related to the increasing content of Fe²⁺ active site, that promoting the excitation of Fe-O cluster [41,42]. Besides, the significant increase of absorbance in visible region on M-350

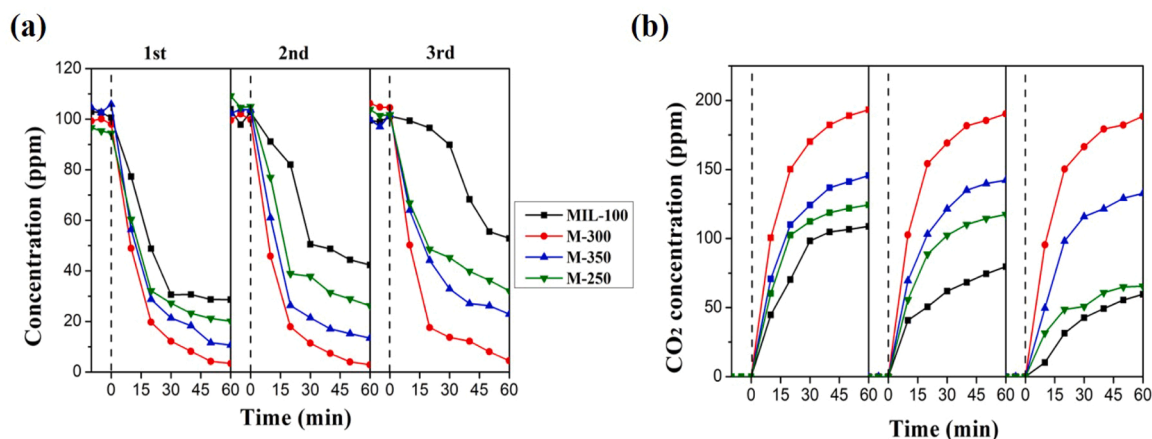


Fig. 3. Photocatalytic performance of (a) acetaldehyde degradation and (b) CO₂ generation.

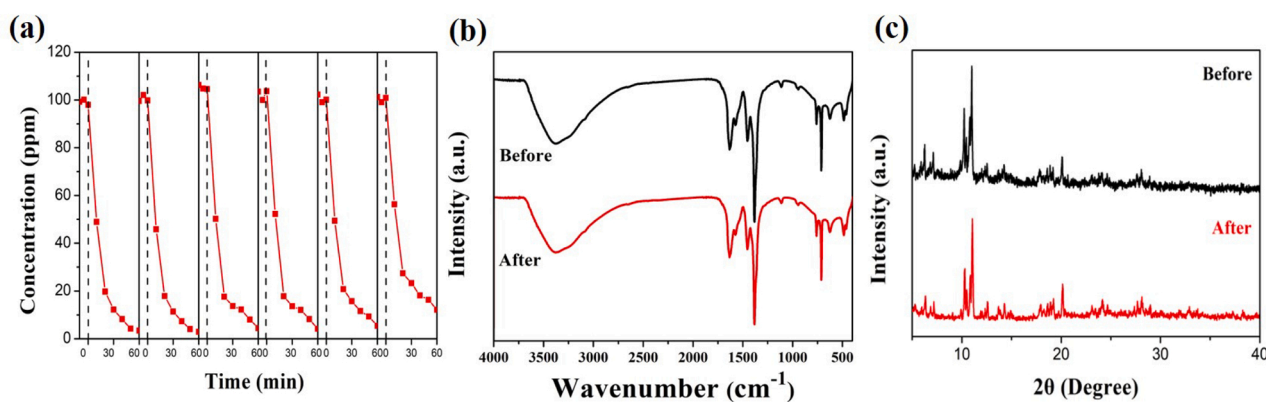


Fig. 4. (a) Photocatalytic performance of acetaldehyde degradation for 6 cycles; (b) FT-IR spectra and (c) XRD pattern of M-300 before and after 6 recycling photocatalytic degradation of acetaldehyde.

might because of the high degree of carbonization, the carbon would enhance the absorbance of visible light [43]. In addition, the Tauc curves (Fig. 2b) obtained from UV-vis spectra showed the bandgap energies of MIL-100, M-250, M-300 and M-350 were 2.90, 2.89, 2.89 and 2.87 eV, respectively. Mott-Schottky curve was used to measure the flat band potential (E_{FB}). As shown in Fig. S6, the E_{FB} of M-300 was -0.05 V vs. NHE. The positive slope of the curve confirmed that M-300 was an n-type semiconductor, the conduction band (E_{CB}) of n-type semiconductor was about 0.1 V negative than the E_{FB} [7]. Thus, the E_{CB}

of M-300 was -0.15 V. The valence band energy (E_{VB}) of M-300 was calculated to be 2.74 V according to the band gap energy.

To further explore the electron transfer behavior on catalyst, photo response current was carried out. As shown in Fig. 2c, compared with precursor MIL-100(Fe), the photo response currents of derivatives increased obviously with the increase of the temperature of thermal treatment. And M-350 exhibited the highest current intensity, which might be related to the highest carbonization. The carbon formed during the thermal treatment process could greatly increase the conductivity,

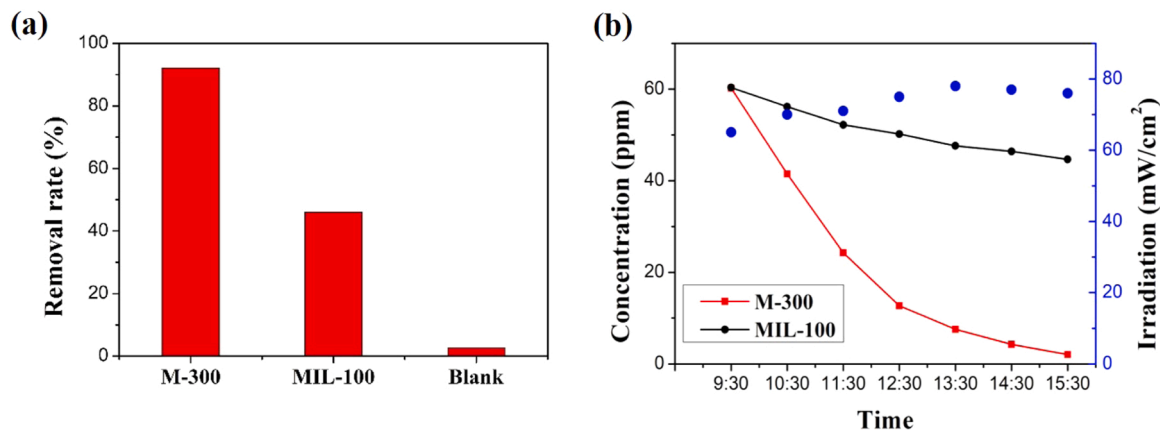


Fig. 5. (a) E. coli removal rate under the visible light and (b) photocatalytic performance of acetaldehyde degradation under the sunlight. Location: N 23°3'0.11''-E 113°24'51.27''.

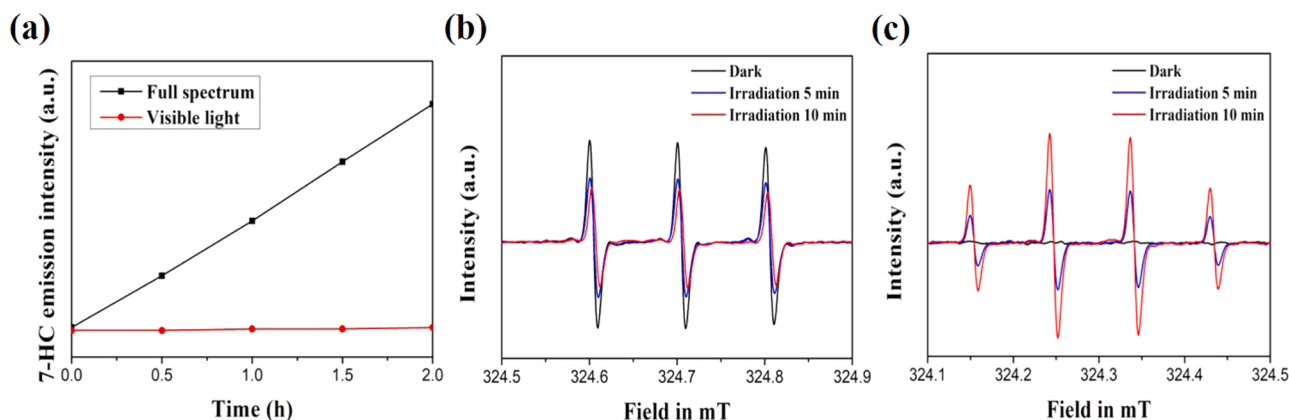


Fig. 6. (a) Time profile of 7-hydroxycoumarin (7-HC); (b) ESR spectra (TEMPO spin-trapping) for M-300 under dark and visible light and (c) ESR spectra (DMPO spin-trapping) for M-300 under dark and visible light for DMPO-OH.

enhance the photocurrent intensity, and further improve the charge transfer efficiency in a certain range [14,43]. Therefore, although M-300 had the highest $\text{Fe}^{2+}/\text{Fe}^{3+}$ ratio, the degree of carbonization of M-350 is higher than that of M-300, which highly increased the photocurrent intensity of M-350. The electrochemistry impedance spectroscopy (EIS) results in Fig. 2d were consistent with the photocurrent results. These indicated that Fe-MOF derivatives with mixed valence state of $\text{Fe}^{2+}/\text{Fe}^{3+}$ obtained by thermal treatment of MIL-100(Fe) could significantly enhance the separation efficiency of photogenerated electron-hole and the electron transfer, which was of great significance for photocatalytic activity.

3.3. Photocatalytic performance

The photocatalytic activity was evaluated by static photocatalytic degradation of acetaldehyde under visible light. As shown in Fig. 3a and b, the activity of pure MIL-100(Fe) decreased gradually in 3 cycles. On the contrary, the derivatives showed better photocatalytic performance of acetaldehyde degradation and higher CO_2 generation. Interestingly, although M-350 had higher photocurrent and smaller electrochemical impedance, M-300 exhibited higher activity and stability. With the increase of cycle times, the performance of MIL-100(Fe), M-250 and M-350 decreased gradually. All these results manifested that the conductivity of catalyst was not the only factor for the improvement of photocatalytic efficiency.

In addition, when M-300 was illuminated without acetaldehyde, only a small amount of CO_2 was detected (Fig. S7), which may due to the oxidation of residual ethanol during the coating process. As shown in Fig. 4a, M-300 was repeatable 6 times with no significant reduction in activity. According to the FT-IR and XRD patterns after the reaction, no obvious change was found and the chemical structure of M-300 was stable (Fig. 4b and c).

Pathogenic aerosols are also the major indoor pollutants. To investigate the indoor purification capacity of M-300 more comprehensively, it was necessary to investigate its antibacterial activity. As shown in Fig. 5a, *E. coli* barely decreased under visible light only, and M-300 could achieve more than 90 % removal rate of *E. coli* under visible light (Fig. S8), while the removal rate of its precursor was only less than 50 %. These results showed that M-300 also had excellent antibacterial performance.

Moreover, in order to be closer to the actual application, the degradation of acetaldehyde was also evaluated under the sunlight (Fig. 5b). M-300 also exhibited higher activity than the precursor MIL-100(Fe). This further proved that M-300 had the great potential for practical application.

3.4. Mechanism analysis

According to the evaluation of photocatalytic performance, we found that M-350 with the highest photocurrent and the smallest electrochemical impedance did not exhibit the highest activity, which indicated that the conductivity of the catalyst itself was not the decisive factor to the enhancement of photocatalytic efficiency. In fact, during the photocatalytic degradation of pollutants, the photocatalyst produces the photogenerated electrons and holes under the light excitation. Only the photogenerated holes obtain the electrons from pollutants and the photogenerated electrons reach the other electron acceptors, thus the separation of photogenerated electrons and holes can be realized. Therefore, it is necessary to clarify the mechanism of half-reaction on oxidation and reduction during the photocatalytic process.

We first investigated the oxidation cycles. In addition to oxidizing the pollutants, photogenerated holes could also generate $\bullet\text{OH}$ or other radical species. M-300 was dispersed in coumarin solution, the $\bullet\text{OH}$ was captured by coumarin and formed 7-hydroxycoumarin (7-HC). The free state $\bullet\text{OH}$ was verified by detecting the signal of 7-HC in the solution. Under visible light, no signal of 7-HC was detected, while when in full spectrum light irradiation, the product 7-HC was detected (Fig. 6a). It might because $\bullet\text{OH}$ produced by holes (h^+) under visible light was adsorbed on the surface of M-300 and the light energy was too low to release $\bullet\text{OH}$ into the solution and to be captured by coumarin.

To prove this opinion, electron spin-resonance spectroscopy (ESR) was carried out to detect the photogenerated h^+ and $\bullet\text{OH}$. 2,2,6,6-Tetramethylpiperidine 1-oxyl (TEMPO) and 2,2-dimethyl-3,4-dihydro-2H-pyrrole 1-oxide (DMPO) were used as trapping probes of h^+ and $\bullet\text{OH}$, respectively. As shown in Fig. 6b, the TEMPO signal could be observed in dark condition. Under visible light, TEMPO reacted with h^+ , so the signal gradually decreased with the illumination time went by, which proved the existence of h^+ . DMPO-OH signal was also detected under the visible light illumination, which suggested that $\bullet\text{OH}$ was generated under visible light (Fig. 6c).

In most cases, O_2 is the only electron acceptor in the photocatalytic degradation of pollutants, and the transfer rate of photogenerated electrons to O_2 is crucial for the improvement of photocatalytic oxidation efficiency. In this study, the Fe^{2+} sites work as a bridge to transfer the photo-generated electron to the adsorbed O_2 . If the photo-generated electron reaches the Fe^{2+} sites and stay into the empty orbitals in excited-state, the Fe^{2+} will reduce into Fe^+ . The Fe^+ contains an excited electron, which has a higher energy level, it indicates that Fe^+ has lower overpotential of O_2 reduction [44,45]. Therefore, to verify whether Fe^{2+} is reduced into Fe^+ during the photocatalysis, the ORR of M-300 in dark and irradiation conduction were carried out. The current density of oxygen reduction significantly increased but the onset potential changed slightly under irradiation, which explained that in the process of

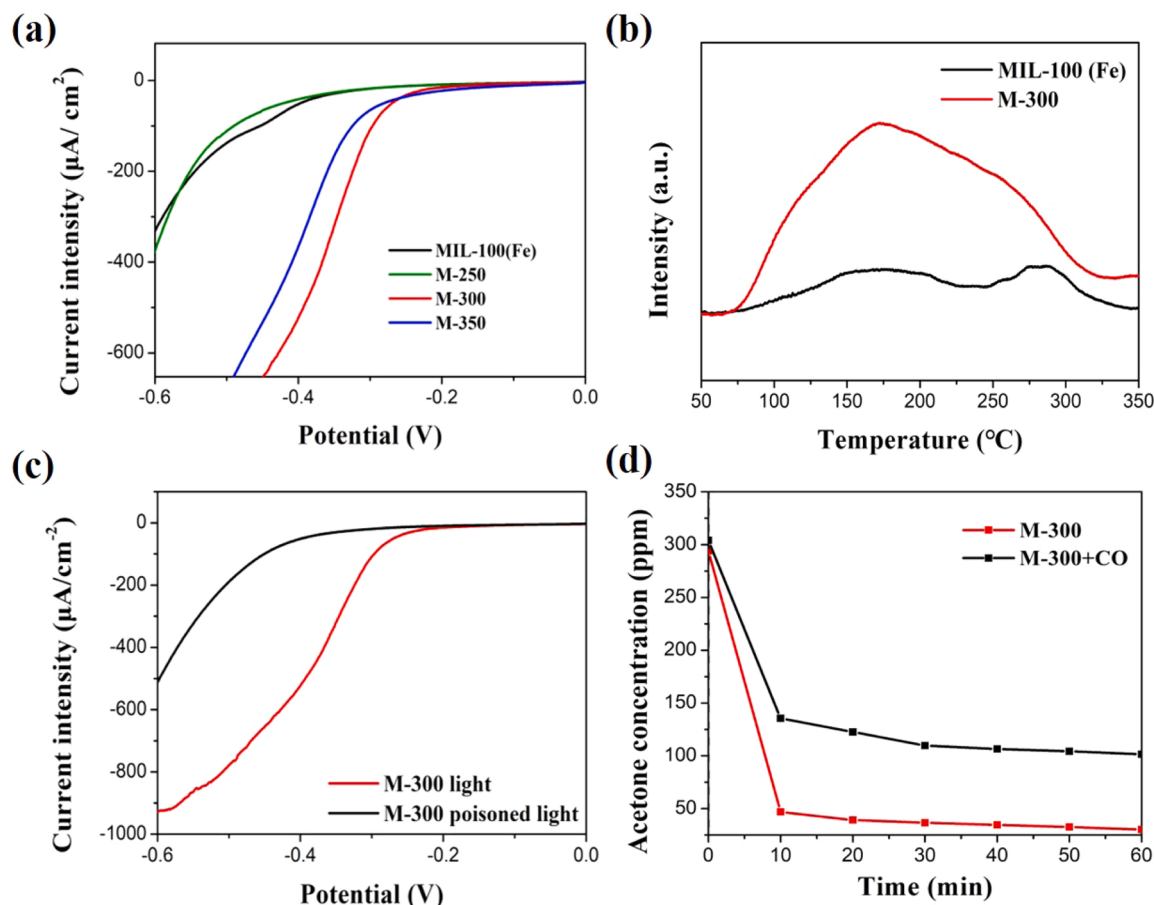


Fig. 7. (a) ORR curve of MIL-100(Fe), M-250, M-300 and M-350 under the visible light; (b) the CO-TPD of MIL-100(Fe) and M-300 after poisoned by CO; (c) the ORR curve of M-300 after poisoned by CO under the visible light; (d) photocatalytic degradation of acetone by M-300 treated with CO poisoning.

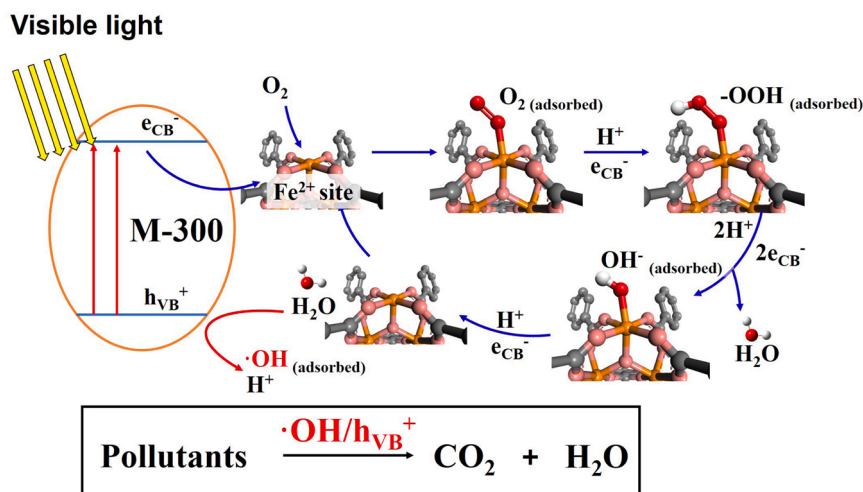
photocatalysis most of the photogenerated electrons were transferred to the O_2 directly rather than reduced Fe^{2+} into Fe^+ (Fig. S9). As shown in Fig. 7a, M-300 had the lowest onset potential of O_2 reduction compared with other samples, which indicated that the Fe^{2+} sites significantly reduced the oxygen reduction overpotential and promoted the charge separation. Before the onset potential, the current intensity of M-350 was slightly higher than that of M-300, which might be attributed to the higher conductivity of M-350. The ORR curves of MIL-100(Fe) and M-250 were similar. These results were consistent with the performance of photocatalytic experiments, which indicated that the oxygen reduction capacity of the material played an important role in the degradation of pollutants. Notably, the ORR activity was also correlated with the Fe^{2+}/Fe^{3+} in the previous XPS characterization, which suggested that the unsaturated Fe^{2+} site might act as the active site in the oxygen reduction process. Therefore, that is why the mixed valence state of Fe^{2+}/Fe^{3+} promotes charge separation.

We also notice that the Fe^{3+} species is dominate after thermal treatment. Although the thermal treatment can break the Fe-OH or Fe-F bonds and release the unsaturated active sites, the samples will inevitably contact with air after the treatment and the unsaturated Fe^{2+} sites are occupied by O_2 [46]. Thus, the amount of Fe^{2+} species on M-300 obtained from XPS spectrum is lower than that before contact with air. The binding of O_2 and Fe^{2+} site is reversible [47], and it is also a part of the photocatalysis reaction, so it will not decrease the activity of samples.

To verify the amount of unsaturated Fe^{2+} sites on M-300 after thermal treatment, we used CO as a probe molecule to occupy the Fe^{2+} sites and replace the Fe- O_2 bond, the interaction between CO and Fe^{3+} was weak in room temperature, but there was a strong bond force

between CO and Fe^{2+} [24]. To evaluate the relative quantity of Fe^{2+} sites before and after the thermal treatment, MIL-100(Fe) and M-300 were poisoning in 10% CO stream, the content of Fe^{2+} sites was determined by CO-TPD. M-300 showed obvious CO desorption signal at 80–300 °C while MIL-100(Fe) showed only a small amount of CO desorption signal (Fig. 7b). This suggested that M-300 had much more unsaturated Fe^{2+} sites than MIL-100. The ORR test and the photocatalytic degradation of acetone were also carried out for poisoned M-300. Acetone was selected as the model VOC molecule because it was easy to react with $\bullet OH$ [48], thus it could reflect the influence of poisoning on photocatalytic activity more sensitively. As shown in Fig. 7c, the ORR performance was significantly decreased after being poisoned by CO, the onset potential was at about -0.45 V, which was similar to those of MIL-100(Fe) and M-250 that had few Fe^{2+} . As was the case with ORR, the photocatalytic performance also decreased after being poisoned by CO (Fig. 7d). The above results demonstrated that M-300 had a higher content of Fe^{2+} sites, which facilitated the adsorption of O_2 and the transfer of photogenerated electrons from M-300 to O_2 . The promotion to the reduction cycle by M-300 also improved the efficiency of the entire photocatalytic reaction.

To clarify the pathway of the O_2 reduction when obtaining the photogenerated electrons, we also used NBT as a probe to detect the formation of $O_2\bullet^-$. The result (Fig. S10) showed that no free $O_2\bullet^-$ generated during the illumination, which was consistent with the characterization of the band gap structure. The potential of $O_2/O_2\bullet^-$ is -0.3 V vs. NHE, and the E_{CB} of M-300 band do not have enough potential to produce $O_2\bullet^-$. Similarly, no H_2O_2 was detected by MnO_4^- probe (Fig. S11), which suggested that O_2 adsorbed on M-300 was eventually reduced to H_2O by a 4-electron transfer pathway [45]. Besides, a small



Scheme 1. The mechanism for photocatalytic oxidation on M-300 catalyst under visible light.

amount of H_2O_2 was found in MIL-100(Fe), indicating that part of the O_2 adsorbed on the MIL-100(Fe) was reduced to H_2O_2 through a 2-electron transfer pathway, whose transfer rate was slower than that in M-300 [49].

Based on the above results, the photocatalytic mechanism of M-300 was proposed in Scheme 1. The band gap of M-300 was 2.89 eV, and the E_{CB} and E_{VB} were -0.15 and 2.74 V, respectively. Firstly, M-300 generated electron-hole pairs under visible light. The photogenerated hole at the valence band degraded pollutants directly, or reacted with water and formed $\cdot\text{OH}$ which would be adsorbed on the surface of the catalyst. The electrons on the conduction band of M-300 didn't have enough potential to produce free $\cdot\text{O}_2$. Therefore, the abundant unsaturated Fe^{2+} sites on M-300 provided sufficient adsorption sites, which could reduce O_2 to H_2O_2 through a 4-electron pathway (Scheme 1).

4. Conclusions

In summary, a series of derivatives (M-250, M-300 and M-350) with $\text{Fe}^{2+}/\text{Fe}^{3+}$ mixed valence Fe sites were prepared by thermal treatment of MIL-100(Fe) at different temperatures, and used for VOC degradation and bacteriostatic test of *E. coli* under visible light. Compared with the precursor MIL-100(Fe), the derivatives exhibited enhanced activity in acetaldehyde degradation, and M-300 had the best photocatalytic performance and stability. The thermal treatment produced more unsaturated Fe^{2+} activity sites, which effectively promoted the adsorption of O_2 and the transfer of photogenerated electron, thereby significantly improving the efficiency of photocatalytic oxidation. It further proved that the improvement in half-reaction of reduction could promote the entire efficiency of photocatalytic oxidation reaction. Moreover, M-300 also showed a good antibacterial performance under visible light and an excellent activity for acetaldehyde degradation under the sunlight, suggesting an application prospect in the field of indoor air purification.

CRediT authorship contribution statement

Junxian Qin: Investigation, Visualization, Writing – original draft, Writing – review & editing, Formal analysis. **Yun Pei:** Investigation, Visualization, Writing – original draft. **Yue Zheng:** Visualization, Writing – review & editing. **Daiqi Ye:** Formal analysis, Conceptualization. **Yun Hu:** Writing – original draft, Writing – review & editing, Formal analysis, Supervision, Conceptualization.

Declaration of Competing Interest

The authors declare that they have no known competing financial

interests or personal relationships that could have appeared to influence the work reported in this paper.

Data Availability

Data will be made available on request.

Acknowledgements

This work was supported by National Natural Science Foundation of China (21777047), the Science and Technology Project of Guangdong Province (2022A0505050002), Scientific Research Project of Guangzhou City (201804020026) and the Science and Technology Program of Guangzhou (202002020020).

Supplementary Material

The supplementary material contains the characterization methods of SEM, XRD, UV-vis, FTIR, XPS, ESR, the details of photoelectrochemical and photochemical measurements, temperature-programmed desorption of CO, the cycling experiments of M-300, the characterization of M-300 after the reaction, the digital pictures of colony-forming unit of *E. coli* and the experiment of radicals ($\text{O}_2\cdot^-$ and H_2O_2).

Appendix A. Supporting information

Supplementary data associated with this article can be found in the online version at [doi:10.1016/j.apcatb.2022.122346](https://doi.org/10.1016/j.apcatb.2022.122346).

References

- [1] W. Zhang, G. Li, H. Yin, K. Zhao, H. Zhao, T. An, Adsorption and desorption mechanism of aromatic VOCs onto porous carbon adsorbents for emission control and resource recovery: recent progress and challenges, *Environ. Sci.: Nano* 9 (2022) 81–104, <https://doi.org/10.1039/D1EN00929J>.
- [2] S. Brosillon, M.-H. Manero, J.-N. Foussard, Mass transfer in VOC adsorption on zeolite: experimental and theoretical breakthrough curves, *Environ. Sci. Technol.* 35 (2001) 3571–3575, <https://doi.org/10.1021/es010017x>.
- [3] M. Wen, G. Li, H. Liu, J. Chen, T. An, H. Yamashita, Metal-organic framework-based nanomaterials for adsorption and photocatalytic degradation of gaseous pollutants: recent progress and challenges, *Environ. Sci.: Nano* 6 (2019) 1006–1025, <https://doi.org/10.1039/C8EN01167B>.
- [4] Y. Wang, Y. Zhang, X. Zhu, Y. Liu, Z. Wu, Fluorine-induced oxygen vacancies on TiO_2 nanosheets for photocatalytic indoor VOCs degradation, *Appl. Catal. B* 316 (2022) 121610, <https://doi.org/10.1016/j.apcatb.2022.121610>.
- [5] H. Li, H. Gong, Z. Jin, Phosphorus modified Ni-MOF-74/ BiVO_4 S-scheme heterojunction for enhanced photocatalytic hydrogen evolution, *Appl. Catal. B* 307 (2022) 121166, <https://doi.org/10.1016/j.apcatb.2022.121166>.

- [6] J. Zhang, Z. Guo, Z. Yang, J. Wang, J. Xie, M. Fu, Y. Hu, TiO₂@UiO-66 composites with efficient adsorption and photocatalytic oxidation of VOCs: investigation of synergistic effects and reaction mechanism, *ChemCatChem* 13 (2021) 581–591, <https://doi.org/10.1002/cctc.202001466>.
- [7] Q. Huang, Y. Hu, Y. Pei, J. Zhang, M. Fu, In situ synthesis of TiO₂@NH₂-MIL-125 composites for use in combined adsorption and photocatalytic degradation of formaldehyde, *Appl. Catal. B* 259 (2019), 118106, <https://doi.org/10.1016/j.apcatb.2019.118106>.
- [8] S.S.A. Shah, T. Najam, M.K. Aslam, M. Ashfaq, M.M. Rahman, K. Wang, P. Tsiakaras, S. Song, Y. Wang, Recent advances on oxygen reduction electrocatalysis: correlating the characteristic properties of metal organic frameworks and the derived nanomaterials, *Appl. Catal. B* 268 (2020), 118570, <https://doi.org/10.1016/j.apcatb.2019.118570>.
- [9] W. Zhang, Y. Hu, J. Ge, H.L. Jiang, S.H. Yu, A facile and general coating approach to moisture/water-resistant metal-organic frameworks with intact porosity, *J. Am. Chem. Soc.* 136 (2014) 16978–16981, <https://doi.org/10.1021/ja509960n>.
- [10] K. Shen, X. Chen, J. Chen, Y. Li, Development of MOF-derived carbon-based nanomaterials for efficient catalysis, *ACS Catal.* 6 (2016) 5887–5903. DOI: [acscatal.6b01222](https://doi.org/10.1021/acscatal.6b01222).
- [11] N.-X. Zhu, Z.-W. Wei, C.-X. Chen, X.-H. Xiong, Y.-Y. Xiong, Z. Zeng, W. Wang, J.-J. Jiang, Y.-N. Fan, C.-Y. Su, High water adsorption MOFs with optimized pore-nanospaces for autonomous indoor humidity control and pollutants removal, *Angew. Chem. Int. Ed.* 133 (2021), e202112097, <https://doi.org/10.1002/anie.202112097>.
- [12] Z. Ye, J.A. Padilla, E. Xuriguera, J.L. Beltran, F. Alcaide, E. Brillas, I. Sires, A highly stable metal-organic framework-engineered FeS₂/C nanocatalyst for heterogeneous electro-fenton treatment: validation in wastewater at mild pH, *Environ. Sci. Technol.* 54 (2020) 4664–4674, <https://doi.org/10.1021/acs.est.9b07604>.
- [13] J. Tang, J. Wang, Metal organic framework with coordinatively unsaturated sites as efficient Fenton-like catalyst for enhanced degradation of sulfamethazine, *Environ. Sci. Technol.* 52 (2018) 5367–5377, <https://doi.org/10.1021/acs.est.8b00092>.
- [14] J. Qin, J. Wang, J. Yang, Y. Hu, M. Fu, D. Ye, Metal organic framework derivative-TiO₂ composite as efficient and durable photocatalyst for the degradation of toluene, *Appl. Catal. B* 267 (2020), 118667, <https://doi.org/10.1016/j.apcatb.2020.118667>.
- [15] X. Chen, X. Peng, L. Jiang, X. Yuan, J. Fei, W. Zhang, Photocatalytic removal of antibiotics by MOF-derived Ti³⁺- and oxygen vacancy-doped anatase/rutile TiO₂ distributed in a carbon matrix, *Chem. Eng. J.* 427 (2022), 130945, <https://doi.org/10.1016/j.cej.2021.130945>.
- [16] C. Zhang, M. Jia, Z. Xu, W. Xiong, Z. Yang, J. Cao, H. Peng, H. Xu, Y. Xiang, Y. Jing, Constructing 2D/2D N-ZnO/g-C₃N₄ S-scheme heterojunction: efficient photocatalytic performance for norfloxacin degradation, *Chem. Eng. J.* 430 (2022), 132652, <https://doi.org/10.1016/j.cej.2021.132652>.
- [17] P.V. Kamat, S. Jin, Semiconductor photocatalysis: “tell us the complete story”, *ACS Energy Lett.* 3 (2018) 622–623, <https://doi.org/10.1021/acsenenergylett.8b00196>.
- [18] W. Sun, Q. Meng, L. Jing, D. Liu, Y. Cao, Facile synthesis of surface-modified nanosized α-Fe₂O₃ as efficient visible photocatalysts and mechanism insight, *J. Phys. Chem. C* 117 (2013) 1358–1365, <https://doi.org/10.1021/jp309599d>.
- [19] L. Kurfirtová, Y.-K. Seo, Y.K. Hwang, J.-S. Chang, J. Čejka, High activity of iron containing metal-organic-framework in acylation of p-xylene with benzoyl chloride, *Catal. Today* 179 (2012) 85–90, <https://doi.org/10.1016/j.cattod.2011.08.001>.
- [20] A. Dhakshinamoorthy, M. Alvaro, P. Horcajada, E. Gibson, M. Vishnuvarthan, A. Vimont, J.-M. Grenèche, C. Serre, M. Daturi, H. Garcia, Comparison of porous iron trimesates basolite F300 and MIL-100(Fe) as heterogeneous catalysts for Lewis acid and oxidation reactions: roles of structural defects and stability, *ACS Catal.* 2 (2012) 2060–2065, <https://doi.org/10.1021/cs300345b>.
- [21] Y. Pei, J. Qin, J. Wang, Y. Hu, Fe-based metal organic framework derivative with enhanced Lewis acidity and hierarchical pores for excellent adsorption of oxygenated volatile organic compounds, *Sci. Total Environ.* 790 (2021), 148132, <https://doi.org/10.1016/j.scitotenv.2021.148132>.
- [22] D. Wang, R. Huang, W. Liu, D. Sun, Z. Li, Fe-based MOFs for photocatalytic CO₂ reduction: role of coordination unsaturated sites and dual excitation pathways, *ACS Catal.* 4 (2014) 4254–4260, <https://doi.org/10.1021/cs501169t>.
- [23] L. Wang, X. Zhang, X. Yu, F. Gao, Z. Shen, X. Zhang, S. Ge, J. Liu, Z. Gu, C. Cheng, An all-organic semiconductor C3N₄/PDINH heterostructure with advanced antibacterial photocatalytic therapy activity, *Adv. Mater.* 31 (2019), 1901965, <https://doi.org/10.1002/adma.201901965>.
- [24] J.W. Yoon, Y.K. Seo, Y.K. Hwang, J.S. Chang, H. Leclerc, S. Wuttke, P. Bazin, A. Vimont, M. Daturi, E. Bloch, Controlled reducibility of a metal-organic framework with coordinatively unsaturated sites for preferential gas sorption, *Angew. Chem. Int. Ed.* 49 (2010) 5949–5952, <https://doi.org/10.1002/anie.201001230>.
- [25] M. Nehra, N. Dilbaghi, N.K. Singhal, A.A. Hassan, K.-H. Kim, S. Kumar, Metal organic frameworks MIL-100(Fe) as an efficient adsorptive material for phosphate management, *Environ. Res.* 169 (2019) 229–236, <https://doi.org/10.1016/j.envres.2018.11.013>.
- [26] S. Huang, K.L. Yang, X.F. Liu, H. Pan, H. Zhang, S. Yang, MIL-100(Fe)-catalyzed efficient conversion of hexoses to lactic acid, *RSC Adv.* 7 (2017) 5621–5627, <https://doi.org/10.1039/C6RA26469G>.
- [27] N.M. Mahmoodi, J. Abdi, M. Oveis, M.A. Asli, M. Vossoughi, Metal-organic framework (MIL-100 (Fe)): synthesis, detailed photocatalytic dye degradation ability in colored textile wastewater and recycling, *Mater. Res. Bull.* 100 (2018) 357–366, <https://doi.org/10.1016/j.materresbull.2017.12.033>.
- [28] F. Zhang, J. Shi, Y. Jin, Y. Fu, Y. Zhong, W. Zhu, Facile synthesis of MIL-100(Fe) under HF-free conditions and its application in the acetalization of aldehydes with diols, *Chem. Eng. J.* 259 (2015) 183–190, <https://doi.org/10.1016/j.cej.2014.07.119>.
- [29] Y.-K. Seo, J.W. Yoon, J.S. Lee, U.-H. Lee, Y.K. Hwang, C.-H. Jun, P. Horcajada, C. Serre, J.-S. Chang, Large scale fluorine-free synthesis of hierarchically porous iron(III) trimesate MIL-100(Fe) with a zeolite MTN topology, *Microporous Mesoporous Mater.* 157 (2012) 137–145, <https://doi.org/10.1016/j.micromeso.2012.02.027>.
- [30] K. Suwelack, D. Wuest, M. Zeller, A. Kruse, J. Kruempel, Hydrothermal carbonization of wheat straw—prediction of product mass yields and degree of carbonization by severity parameter, *Biomass Convers. Bioref.* (2022), <https://doi.org/10.1007/s13399-022-03644-1>.
- [31] X. Zheng, L. Zhang, Z. Fan, Y. Cao, L. Shen, C. Au, L. Jiang, Enhanced catalytic activity over MIL-100(Fe) with coordinatively unsaturated Fe²⁺/Fe³⁺ sites for selective oxidation of H₂S to sulfur, *Chem. Eng. J.* 374 (2019) 793–801, <https://doi.org/10.1016/j.cej.2019.05.228>.
- [32] M. Tong, D. Liu, Q. Yang, S. Influence of framework metal ions on the dye capture behavior of MIL-100 (Fe, Cr) MOF type solids, *J. Mater. Chem. A* 1 (2013) 8534–8537, <https://doi.org/10.1039/C3TA11807J>.
- [33] F. Zhang, Y. Jin, J. Shi, Y. Zhong, W. Zhu, M.S. El-Shall, Polyoxometalates confined in the mesoporous cages of metal-organic framework MIL-100(Fe): efficient heterogeneous catalysts for esterification and acetalization reactions, *Chem. Eng. J.* 269 (2015) 236–244, <https://doi.org/10.1016/j.cej.2015.01.092>.
- [34] M. Ahmad, X. Quan, S. Chen, H. Yu, Tuning Lewis acidity of MIL-88B-Fe with mix-valence coordinatively unsaturated iron centers on ultrathin Ti₃C₂ nanosheets for efficient photo-Fenton reaction, *Appl., Catal., B* 264 (2020), 118534, <https://doi.org/10.1016/j.apcatb.2019.118534>.
- [35] Y. Fang, Z. Yang, H. Li, X. Liu, MIL-100(Fe) and its derivatives: from synthesis to application for wastewater decontamination, *Environ. Sci. Pollut. Res.* 27 (2020) 4703–4724, <https://doi.org/10.1007/s11356-019-07318-w>.
- [36] H. Zhang, H. Wang, Z. Pan, Z. Wu, Y. Deng, J. Xie, J. Wang, X. Han, W. Hu, Zn-metal-organic framework derived ordered mesoporous carbon-based nanostructure for high-performance and universal multivalent metal ion storage, *Adv. Mater.* (<https://doi.org/10.1002/adma.202206277>).
- [37] P. Horcajada, S. Surblé, C. Serre, D. Hong, Y. Seo, J. Chang, J. Grenèche, I. Margiolaki, G. Férey, Synthesis and catalytic properties of MIL-100(Fe), an iron (iii) carboxylate with large pores, *Chem. Commun.* 27 (2007) 2820–2822, <https://doi.org/10.1039/b704325b>.
- [38] M.V. Parkes, D.F. Sava Gallis, J.A. Greathouse, T.M. Nenoff, Effect of metal in M₃(btc)₂ and M₂(dobdc) MOFs for O₂/N₂ separations: a combined density functional theory and experimental study, *J. Phys. Chem. C* 119 (2015) 6556–6567, <https://doi.org/10.1021/jp511789g>.
- [39] X. Liu, R. Dang, W. Dong, X. Huang, J. Tang, H. Gao, G. Wang, A sandwich-like heterostructure of TiO₂ nanosheets with MIL-100(Fe): a platform for efficient visible-light-driven photocatalysis, *Appl. Catal. B* 209 (2017) 506–513, <https://doi.org/10.1016/j.apcatb.2017.02.073>.
- [40] D. Wang, M. Wang, Z. Li, Fe-based metal-organic frameworks for highly selective photocatalytic benzene hydroxylation to phenol, *ACS Catal.* 5 (2015) 6852–6857, <https://doi.org/10.1021/acscatal.5b01949>.
- [41] Y. Fu, D. Sun, Y. Chen, R. Huang, Z. Ding, X. Fu, Z. Li, An amine-functionalized titanium metal-organic framework photocatalyst with visible-light-induced activity for CO₂ reduction, *Angew. Chem. Int. Ed.* 51 (2012) 3364–3367, <https://doi.org/10.1002/anie.201108357>.
- [42] W. Ren, Z. Ai, F. Jia, L. Zhang, X. Fan, Z. Zou, Low temperature preparation and visible light photocatalytic activity of mesoporous carbon-doped crystalline TiO₂, *Appl. Catal. B* 69 (2007) 138–144, <https://doi.org/10.1016/j.apcatb.2006.06.015>.
- [43] G. Huang, F. Zhang, X. Du, Y. Qin, D. Yin, L. Wang, Metal organic frameworks route to in situ insertion of multiwalled carbon nanotubes in Co₃O₄ polyhedra as anode materials for lithium-ion batteries, *ACS Nano* 9 (2015) 1592–1599, <https://doi.org/10.1021/nn506252u>.
- [44] Q. Lv, Z. Zhu, S. Zhao, L. Wang, Q. Zhao, F. Li, L.A. Archer, J. Chen, Semiconducting metal-organic polymer nanosheets for a photoinvoluted Li–O₂ battery under visible light, *J. Am. Chem. Soc.* 143 (2021) 1941–1947, <https://doi.org/10.1021/jacs.0c11400>.
- [45] D. Du, S. Zhao, Z. Zhu, F. Li, J. Chen, Photo-excited oxygen reduction and oxygen evolution reactions enable a high-performance Zn–air battery, *Angew. Chem.* 132 (2020) 18297–18301, <https://doi.org/10.1002/ange.202005929>.
- [46] E.D. Bloch, L.J. Murray, W.L. Queen, S. Chavan, S.N. Maximoff, J.P. Bigi, R. Krishna, V.K. Peterson, F. Grandjean, G.J. Long, B. Smit, S. Bordiga, C.M. Brown, J.R. Long, Selective binding of O₂ over N₂ in a redox-active metal-organic framework with open iron(II) coordination sites, *J. Am. Chem. Soc.* 133 (2011) 14814–14822, <https://doi.org/10.1021/ja205976v>.
- [47] L.J. Murray, M. Dinca, J. Yano, S. Chavan, S. Bordiga, C.M. Brown, J.R. Long, Highly-selective and reversible O₂ binding in Cr₃(1,3,5-benzenetricarboxylate)₂, *J. Am. Chem. Soc.* 132 (2010) 7856–7857, <https://doi.org/10.1021/ja1027925>.
- [48] S. Aloisio, J.S. Francisco, Complexes of hydroxyl and hydroperoxyl radical with formaldehyde, acetaldehyde, and acetone, *J. Phys. Chem. A* 104 (2000) 3211–3224, <https://doi.org/10.1021/jp993789c>.
- [49] D. Guo, R. Shibuya, C. Akiba, S. Saji, T. Kondo, J. Nakamura, Active sites of nitrogen-doped carbon materials for oxygen reduction reaction clarified using model catalysts, *Science* 351 (2016) 361–365, <https://doi.org/10.1126/science.1248832>.